INORGANIC CHEMISTRY FRONTIERS

CCS 中国化学会 CHINESE CHEMICAL SOCIETY

ROYAL SOCIETY OF CHEMISTRY

Synthesis, Structural, and Electronic Properties of $Sr_{1-x}Ca_xPdAs$

Journal:	*Inorganic Chemistry Frontiers*
Manuscript ID	QI-RES-03-2020-000284.R2
Article Type:	Research Article
Date Submitted by the Author:	12-Jun-2020
Complete List of Authors:	Redemann, Benjamin; The Ohio State University, Department of Chemistry and Biochemistry Scudder, Michael; The Ohio State University, Department of Chemistry and Biochemistry Weber, Daniel; Ohio State University, Department of Chemistry and Biochemistry Wang, Yaxian; The Ohio State University, Department of Materials Science and Engineering Windl, Wolfgang; The Ohio State University, Department of Materials Science and Engineering Goldberger, Joshua; The Ohio State University, Chemistry

ARTICLE

Synthesis, Structural, and Electronic Properties of $Sr_{1-x}Ca_xPdAs$

Benjamin W. Y. Redemann,[a] Michael R. Scudder,[a] Daniel Weber,[a] Yaxian Wang,[b] Wolfgang Windl,[b] and Joshua E. Goldberger[a]*

Received 00th January 20xx,
Accepted 00th January 20xx

DOI: 10.1039/x0xx00000x

Layered honeycomb intermetallic phases have attracted considerable research interest due to the wide array of exciting physical properties inherent in these materials. Here, we follow the evolution in structure and electronic properties of a relatively unexplored material system, $Sr_{1-x}Ca_xPdAs$, as the hexagonal PdAs honeycomb layer in SrPdAs distorts into the orthorhombic CaPdAs structure. The Sr-rich compounds (x = 0 to 1/3) form symmetric, hexagonal honeycomb PdAs layers, whereas in the Ca-rich region (x = ½ to 1) the PdAs layers distort into an orthorhombic structure featuring long and short Pd-Pd distances. This distortion occurs when the average Pd-Pd distance falls below 4.21 Å. All compounds are observed to exhibit metallic temperature-dependent resistivity trends. There are no apparent discontinuities indicative of metal-to-insulator transitions and the room temperature resistivity values range from 18 to 180 mΩ cm. In total, this work maps out the structural and electronic phase diagram of $Sr_{1-x}Ca_xPdAs$ compounds.

1. Introduction

Layered honeycomb compounds have attracted an immense amount of research interest, as many of these compounds often host exotic physical phenomena and useful properties. These properties include topological phenomena[1, 2] that has been predicted and/or discovered in many compounds including $BaSn_2$,[3, 4] single layer stannane,[5, 6], axis-dependent conduction polarity in $NaSn_2As_2$[7, 8] and BaCuAs,[9] the discovery of single layer magnetism in CrI_3[10-13] and $CrGeTe_3$[14-16], hydrogenation catalysis in $BaGa_2$[17] and LaCuSi[18], along with superconductivity in MgB_2 (T_c = 39 K)[19], CaAlSi (T_c = 5.7-7.7 K)[20], and SrPtAs (T_c = 2.4 K)[21]. The search and discovery of compounds containing this layered honeycomb structural motif remains a highly active frontier[22].

SrPdAs and CaPdAs are unique layered materials whose crystal structures suggest the possible existence of unique physical phenomena, such as metal-insulator transitions or superconductivity. SrPdAs is isostructural and isoelectronic to SrPtAs, and crystallizes into the hexagonal ZrBeSi structure type, consisting of $PdAs^{2-}$ layers with a honeycomb alternating BN-like framework, separated by Sr^{2+} cations and with 2-layers per unit cell (**Fig. 1a**). In this 2-layer unit cell the Pd atoms in the first layer are directly above the As atoms in the 2nd-layer. CaPdAs crystallizes into an orthorhombic Pnma space group that features a √3 a x 4a superstructure of the SrPdAs unit cell. In CaPdAs, the Pd-As honeycomb distorts in such a way to form hexagons with very short Pd-Pd distances (3.5-3.8 Å) and hexagons with long Pd-Pd distances (4.5 Å) (**Fig. 1b**). Using formal counting rules, one might expect Pd to exist in the highly unusual Pd^{1+} oxidation state with a d^9 configuration. In CaPdAs the instability of this oxidation state is alleviated via a Peierls distortion, which disrupts the in-plane Pd-As bond lengths and angles to splits the degeneracy of the Pd d_{x2-y2} and d_{xy} bands. [23] This distortion is facilitated by the smaller ionic radius of Ca^{2+}. Experimentally, SrPdAs was claimed to be metallic whereas the electrical properties of CaPdAs have yet to measured.[23] Similarly, EuPdAs, which is isostructural to SrPdAs at room temperature, undergoes an unusual electronically-driven isostructural phase transition at 180 K coincident with a partial increase in europium valence from Eu^{2+} to $Eu^{2.4+}$.[24] Therefore, understanding how to control the structural distortions in this prototypical family of layered honeycomb materials is essential for understanding how to access exotic electronic phenomena in these compounds.

In this study, we synthesized for the first time homogeneous $Sr_{1-x}Ca_xPdAs$ alloys and followed the evolution in structure from the hexagonal SrPdAs to the orthorhombic CaPdAs. We find that in the Sr-rich regime when x = 0, 1/6, and 1/3, the hexagonal structure dominates at room temperature. In the Ca rich ratios at x≥1/2, these alloys crystallize into the distorted orthorhombic Pnma structure at room temperature. We elaborate on the increasing structural distortions that occur as the lattice shrinks with greater Ca ratios. We establish the electronic behavior of these compounds using both high-level structure calculations and electronic structure measurement. All compounds have metallic temperature-dependent resistivities, with room temperature values ranging from 18 to 180 mΩ cm. The SrPdAs and CaPdAs end members have the lowest resistivity values, and the increasing resistivity of the Sr/Ca alloy phases is in close agreement with the Nordheim rule. Furthermore, there is no evidence of structural distortions or metal insulator transitions in all compounds for temperatures ranging down to 2 K. Overall, this work fully establishes the

[a] Department of Chemistry and Biochemistry, The Ohio State University, Columbus, OH 43210-1340, United States
[b] Department of Materials Science and Engineering, The Ohio State University, Columbus, Ohio 43210, United States
Electronic Supplementary Information (ESI) available: [details of any supplementary information available should be included here]. See DOI: 10.1039/x0xx00000x

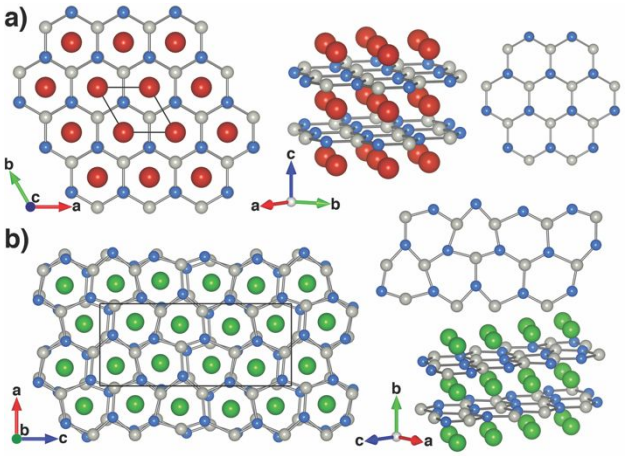

Fig. 1 a) The crystal structure of SrPdAs (Sr=red, Pd=silver, As=blue). Left: the hexagonal, $P6_3/mmc$, unit cell of SrPdAs. Top middle: the structure down the c-axis showing the hexagonally ordered Sr^{2+}. Top right: the structure of the PdAs layer showing the highly symmetric honeycomb PdAs layer. b) The crystal structure of CaPdAs (Ca=green). Left: the orthorhombic, Pnma, unit cell of CaPdAs. Top right: the structure of the distorted PdAs honeycomb layer. Bottom right: the orthorhombic structure down the stacking b-axis.

synthesis, structural changes, and electronic behaviour of this family of compounds.

2. Experimental Section

Synthesis

All $Sr_{1-x}Ca_xPdAs$ powders were synthesized using a sealed quartz tube approach. All of the sample preparation was done in an Ar-filled glovebox. For the two end members SrPdAs, and CaPdAs, stoichiometric amounts of (Sr or Ca):Pd:As with a 7.5% excess of the alkaline earth were placed in an alumina crucible, that was loaded in a quartz tube and sealed under 80 mTorr pressure. These two compounds were heated to 800˚C in a muffle furnace with a 12-15 hour dwell and then cooled to room temperature, in an initial homogenization step. The mixtures were then reground, pelletized, placed in alumina crucibles and resealed. SrPdAs was annealed at 950 ˚C for 10 days. CaPdAs was synthesized according to the procedure,[25] which entailed heating at 850 ˚C for 15 hrs, cooling to room temperature, and repeating this process two more times. Calcium turnings (Ca, Acros Organics, 99%) and strontium pieces (Sr, Strem Chemicals, 99%) were used after the exterior oxide layers were scraped off via mechanical cleavage. Palladium (Pd, Strem Chemicals, 99.95%) and arsenic (As, Strem Chemicals, 99%) powders were used without any further purification steps. The extreme toxicity of As must be always be considered when handling these compounds.

To synthesize the $Sr_{1-x}Ca_xPdAs$ alloys with $1/6 \le x \le 5/6$, stochiometric ratios of all elements were used with no excess alkaline earth elements. The same 12-15 hr 800 ˚C homogenization step described earlier was used for all stoichiometries. The samples were then reground and pelletized, placed in alumina crucibles and sealed in a quartz tube under vacuum. We found that it was essential to vary the synthesis temperature and dwell time for each Sr:Ca stoichiometry to maximize crystallinity, and minimize any trace impurity phases. Explicitly, the x=5/6 alloy was annealed at 875 ˚C for 3 days; the x=2/3 alloy was annealed at 890 ˚C for 10 days; the x=1/2 and 1/3 alloys were annealed at 910 ˚C for 10 days; the x=1/6 alloy was annealed at 920 ˚C for 6 days. We found that annealing at too high a temperature or for too long a time resulted in the formation of impurity phases such as $Sr_{1-x}Ca_xPd_2As_2$, $SrPd_2$ Sr_3As_4, and CaAs. After the final annealing step, all products were found to be air-stable.

Structural Characterization

The crystal structure of the as-grown powders were obtained at room temperature via flat plate powder X-ray diffraction (XRD) measurements using a Bruker D8 powder X-ray diffractometer (sealed Cu X-ray tube: 40 kV and 50 mA). The structures were refined using TOPAS6 Rietveld refinement software.

X-ray fluorescence measurements were collected using an Olympus X-5000 mobile XRF system. Calibration curves using the ratio of Ca Kα to Sr Kα, along with Pd Kα to As Kα were prepared with standards of CaB_6, $SrCO_3$, Pd, and As.

Electronic Structure Calculations

The DFT calculations were done with the Vienna *ab initio* Simulation Package (VASP),[26, 27] using PAW-PBE potentials.[28, 29] A kinetic energy cutoff of 360 eV was used along with 12×12×6 (8×4×4) *k*-mesh for Brillouin zone integration of SrPdAs (CaPdAs) in self-consistent calculations. As the on-site Coulomb interactions for electrons in Pd *d*-orbitals are very strong, we have performed PBE + U calculations within the rotationally invariant Dudarev approach.[30] Calculated U values for Pd in different compounds are typically between 4 eV and 8 eV.[31, 32] Here, we assume an intermediate value of 6 eV for the Pd *4d* orbitals in both CaPdAs and SrPdAs. For CaPdAs and SrPdAs, both the lattice constants and atomic coordinates were fixed to the experimental values, while they were relaxed for bulk Pd, bulk SrAs and the hypothetical Sr_2PdAs_2 phase.

Electronic Transport

Temperature-dependent resistivity measurements of $Sr_{1-x}Ca_xPdAs$ were collected on powders that were pelletized and sintered at 400 ˚C for 2-3 days. Measurements were collected via a four-probe measurement technique using a Quantum Design 14 T Physical Properties Measurement System (PPMS) from 2 to 300 K. Electrical contacts to the pellet was made using Epoxy Technology H2OE silver epoxy, which was cured at 200 ˚C in a fumehood.

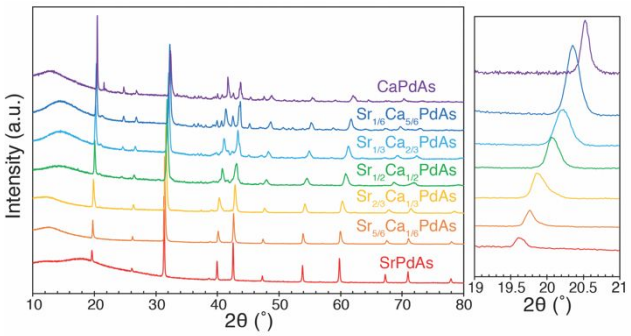

Fig. 2 Left: Offset PXRD patterns of $Sr_{1-x}Ca_xPdAs$ from $0 \le x \le 1$. Samples ranging from $0 \le x \le 1/3$, display the hexagonal $P6_3/mmc$ space group symmetry while samples ranging from $1/2 \le x \le 1$ show the orthorhombic Pnma space group. The transition from the hexagonal to the orthorhombic space group occurs between x=1/3 and x=1/2. Right: The shift in the hexagonal stacking reflection (001) to the orthorhombic stacking reflection (010).

3. Results and Discussion

Pure powders of the SrPdAs and CaPdAs end members were grown via a conventional solid-state synthesis technique. To elucidate the crystal structure of these materials powder XRD pattern was collected (Fig. 2). Rietveld analysis of the diffraction pattern of SrPdAs confirms that it crystallizes into a 2-layer hexagonal $P6_3/mmc$ space group with a = 4.2419(10) Å and c=9.0103(2) Å with no detectable impurities (Fig. S1, Table S1 and S2, ESI†). Each $PdAs^{2-}$ layer is comprised of regular Pd-As hexagons with a Pd-Pd separation of 4.2419 Å (**Fig. 1a**). Rietveld analysis of the CaPdAs diffraction pattern confirms that it crystallizes into a 2-layer orthorhombic Pnma space group with a = 7.136(2) Å, b = 8.640(3) Å, and c = 16.590(5) Å. (Fig. S2, Table S3 and S4, ESI†). In the Pnma space group, the b-axis would correspond to the interlayer stacking axis, while in the $P6_3/mmc$ space group, the c-axis is the interlayer stacking axis. In the Pnma unit cell, the a-axis is rotated by 30° and $\sqrt{3}$x longer than the b-axis of the hexagonal unit cell, while the c-axis is 4x longer and oriented in the same direction as the a-axis of the hexagonal cell (**Fig. 1**). In the orthorhombic space group, the $PdAs^{2-}$ layers form distorted hexagons some of which feature short Pd-Pd distances < 4.2 Å, and some with long Pd-Pd distances > 4.3 Å. Overall, the average Pd-Pd distance in CaPdAs is 4.157 Å, as would be expected considering the smaller ionic radius of Ca^{2+}. Clearly, it is the larger ionic radius of Sr^{2+} that prevents the distortion of the $PdAs^{2-}$ layers in SrPdAs. For reference the 6-coordinate Shannon ionic radii of Sr^{2+} and Ca^{2+} are 1.18 Å and 1.00 Å, respectively.

We subsequently synthesized $Sr_{1-x}Ca_xPdAs$ ($1/6 \le x \le 5/6$) to determine the Sr:Ca stoichiometry at which the $PdAs^{2-}$ layers start to distort. Figure 2 shows the XRD pattern for all of these Sr/Ca alloy phases. The two Sr-rich phases $Sr_{5/6}Ca_{1/6}PdAs$ and $Sr_{2/3}Ca_{1/3}PdAs$ crystallize into the hexagonal $P6_3/mmc$ unit cell (Fig S3, S4, Table S5-S8, ESI†). The orthorhombic distortion becomes apparent in the $Sr_{1/2}Ca_{1/2}PdAs$ phase, by the emergence of new diffraction reflections. Indeed, all $Sr_{1-x}Ca_xPdAs$ phases with $x \ge 1/2$ crystallize into the Pnma space group (Fig S5-S7, Table S9-S14, ESI†). None of the XRD patterns feature additional superstructure reflections indicative of Sr and Ca ordering. Considerable synthetic efforts were spent ensuring that all alloy phases had a homogeneous distribution of Sr and Ca throughout the entire sample. Fig. 2b shows a zoomed region of the XRD pattern highlighting the interlayer diffraction reflection for all $Sr_{1-x}Ca_xPdAs$ phases. This corresponds to either the (002) reflection for the $P6_3/mmc$ unit cells, or the (020) reflection for the Pnma unit cells. The full width half-maximum of this reflection across all samples is <0.2° 2θ indicating the homogeneous distribution of Sr and Ca throughout the samples. The orthorhombic phases all contained a trace undetermined impurity phase with reflections that did not correspond to any known Ca/Sr/Pd/As binary or ternary phase along or oxide phase.

The lattice constants and unit cell volume at different Sr and Ca ratios systematically shift due to the ionic radii differences between Sr^{2+} and Ca^{2+} (Fig. 3). Here, the hexagonal lattice parameters (a_H, b_H, c_H) are converted into the orthorhombic parameters of ($a_o=\sqrt{3}\, b_H$, $b_o=c_H$, $c_o=4\, a_H$). It is apparent that all lattice parameters decrease pseudo-linearly with increasing

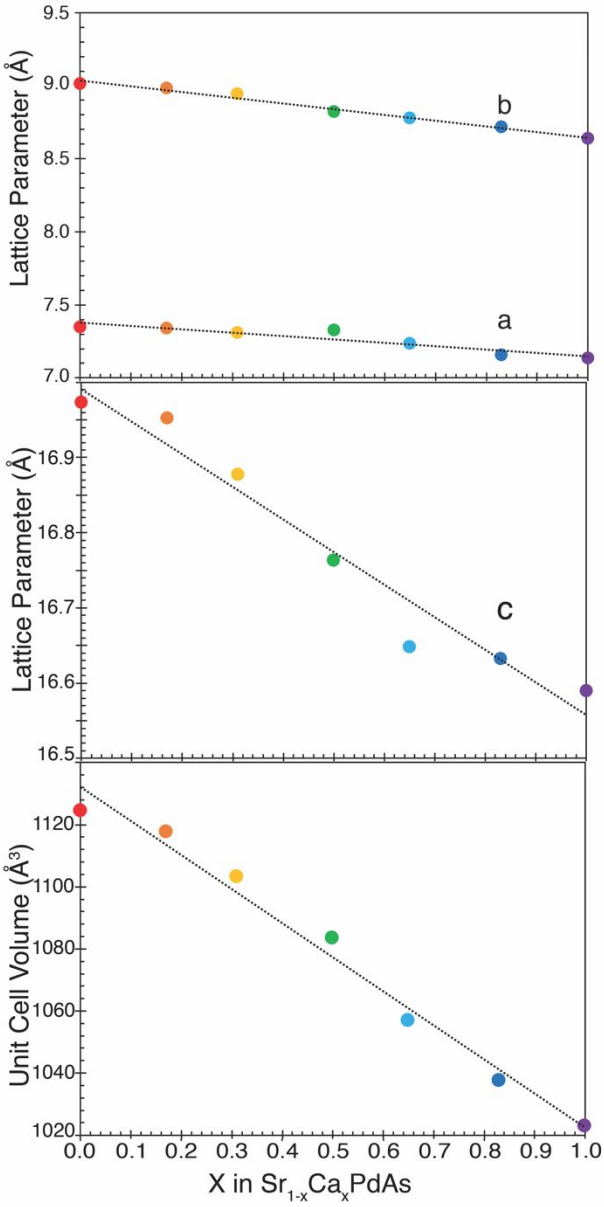

Fig. 3 Top: The a and b lattice parameters decreasing, linearly as the incorporation of calcium increases. Middle: The c lattice parameter decreasing pseudo-linearly as calcium content is increased. Bottom: Unit cell volume decreasing with increasing calcium content characteristic of proper alloying of Sr/Ca.

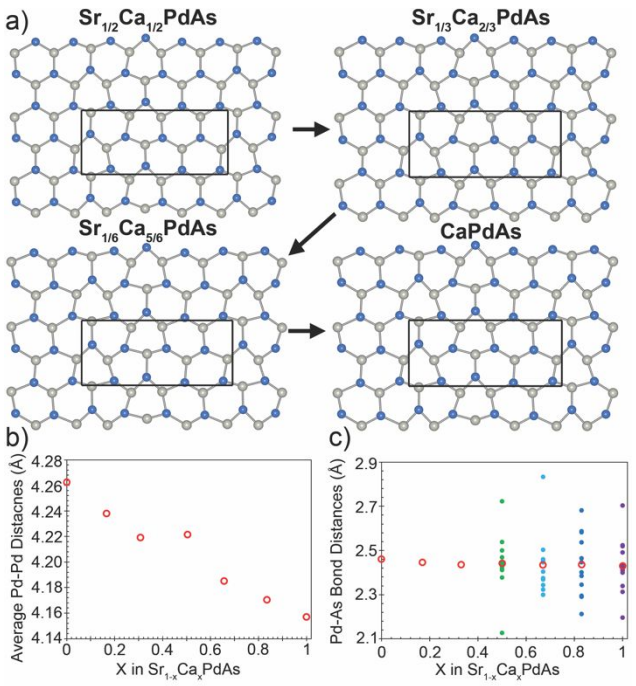

Fig. 4 a) The evolution of the PdAs layers of $Sr_{1-x}Ca_xPdAs$ from ½ ≤ x ≤ 1. The layer distorts from a pseudo-hexagonal PdAs layer to the distorted orthorhombic PdAs layer. b) The average Pd-Pd distances for the alloy phases follow a linear trend as calcium content is increased. c) The Pd-As bond distances in a unit cell of the synthesized phases as well as the average Pd-As distances.

calcium content, in a fashion that would be expected with Vegard's law. Similarly, the unit cell volume decreases with increasing Ca concentration. Again, this is indicative of Sr/Ca alloying into the structure.

There are many layered honeycomb phases that form vacancies rather than incorporate transition metals with unusual oxidation states. For instance, an isostructural SrZnAs phase constructed from ZnAs honeycombs and separated by Sr^{2+} does not exist due to the instablity of Zn^{+}. Instead, half of the Zn atoms on the ZnAs honeycomb are randomly vacant, thereby forming Sr_2ZnAs_2.[33] Thus, due to the formal oxidation state of Pd^{1+}, we considered the possibility of Pd vacancies in the structure. However, XRF measurements indicated a consistent Pd:As ratio of 1:1. Furthermore, when the Pd occupancy was refined in the Rietveld fits, no improvement in the quality of fit was observed. Finally, first principles calculations of the convex hull of the (SrAs)-Pd system indicate that the energy of the Sr_2PdAs_2 crystallized into the hexagonal Sr_2ZnAs_2 structure type with 50% Pd vacancies[33] is 163 meV above the tie line between SrAs (Na_2O_2 structure type, space group $P\bar{6}2m$) and SrPdAs, indicating that the phase is unstable with respect to a two-phase mixture of SrPdAs and SrAs. Details about this calculation are given in the Supplemental Information (Fig S10).

Figure 4 shows the evolution in the PdAs layer starting from $Sr_{0.5}Ca_{0.5}PdAs$, where the orthorhombic cell is first observed, all the way to the CaPdAs phase. In $Sr_{0.5}Ca_{0.5}PdAs$, the change in Pd-As bond lengths and As-Pd-As bond angles start to distort away from an ideal honeycomb geometry. As more Ca is incorporated, the distortion in the PdAs hexagons become more pronounced as more Ca is added. Figure 4b and Figure 4c show the histogram of the intralayer Pd-Pd and intralayer Pd-As bond distances as a function of Ca concentration. First, the average Pd-Pd and Pd-As distances uniformly decrease with increasing Ca concentration. However, the orthorhombic phases all feature Pd-Pd distances and Pd-As distances that show large variances. The Pd-Pd distances can vary from 3.3-4.6 Å, and the Pd-As distances can vary from. 2.1-2.8 Å. These Pd-Pd distances are too large to be indicative of 3 center Pd-Pd-Pd bonding interactions. Finally, while the average As-Pd-As bond angles are 120˚ for all compounds, which reflects the trigonal planar geometry, the average standard deviation of these angles increase from 12.7˚ to 15.7˚ to 19.1˚ to 19.3˚ going from $Sr_{0.5}Ca_{0.5}PdAs$ to CaPdAs.

As established previously by Mewis and Johrendt,[23] a d^9 electron configuration is electronically unstable towards a planar Peierls distortion of the nominally degenerate (d_{xy}, d_{x2-y2}) set, which are the highest energy d-electron bands for this geometry. This Peierls distortion is prevented in SrPdAs due to the large ionic radius of Sr^{2+}. However, once the average ionic radius of the interlayer cation is small enough, the Peierls distortion can occur.

It is interesting to note the early LnPdAs compounds (Ln=La-Eu) all form isostructural hexagonal compounds to SrPdAs.[34] In these compounds where the a-lattice constant / Pd-Pd distance ranges from 4.388 to 4.26 Å. However, GdPdAs and the later, smaller ionic radius lanthanides the compounds form the Pnma TiNiSi structure-type. $Sr_{2/3}Ca_{1/3}PdAs$ is the phase that has the smallest unit cell with a=4.219 Å, before it transforms to the distorted orthorhombic phase. This suggests that the distortions will occur in these hexagonal PdAs layers when the average Pd-Pd distances fall below ~4.21 Å.

After elucidating the structures of $Sr_{1-x}Ca_xPdAs$ via Rietveld analysis, we calculated the electronic structures of SrPdAs and CaPdAs using first principles calculations. Previous calculations had predicted SrPdAs to be a metal and CaPdAs to be a narrow gap semiconductor with Eg ranging from 0.05 to 0.186 eV.[23,35] However, these calculations did not consider the effects of strong electron correlations. Calculated U values for Pd in different configurations typically range between 4 and 8 eV.[31, 32] Here, we assumed an intermediate value of 6 eV.

Our band structure calculations show that both SrPdAs and CaPdAs are metallic, with CaPdAs being a semimetal. (Fig. 5). The density of states of both compounds (Fig. S8-9) indicate that the bands closest to the Fermi level are primarily comprised of Pd 4d and As 4p orbitals, as would be expected for a material with a formal Pd d^9 valence count. The band structure of SrPdAs bears a remarkable resemble to the isostructural d^{10} compounds AeCuPn (Ae = Ca, Sr, Ba; Pn = P, As, Sb),[9] albeit with the Fermi level cutting through the Pd $4d_{xy}/d_{x2-y2}$ – As $4p_x/p_y$ hybrid band, and is indicative of a true metal. However, the Peierls distortion in the √3 a x 4a unit cell of CaPdAs (16 Pd atoms/unit cell) removes the degeneracy of these bands to cause ¾ of the Pd $4d_{xy}/d_{x2-y2}$ – As $4p_x/p_y$ bands to be slightly lower in energy and are valence bands. The remaining higher energy Pd $4d_{xy}/d_{x2-y2}$ – As $4p_x/p_y$ bands comprise the conduction bands.

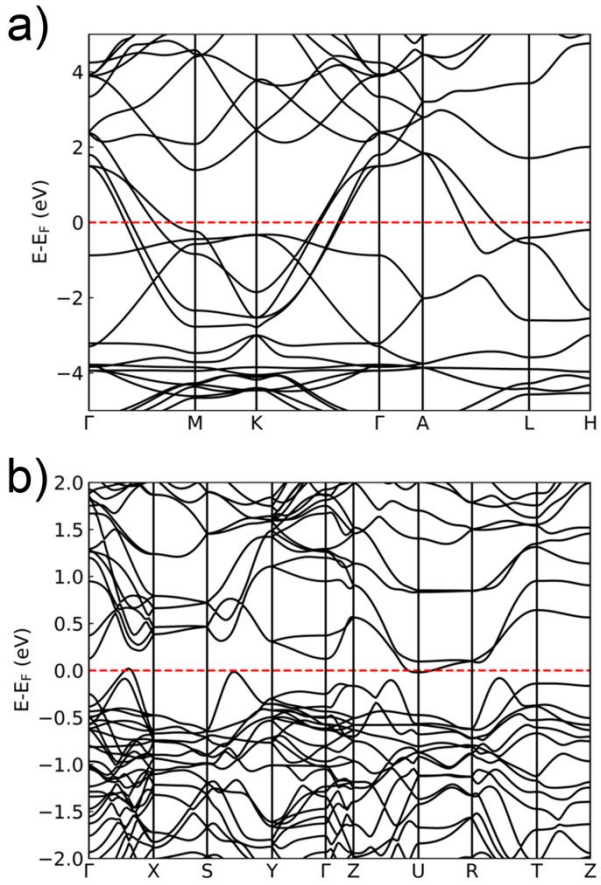

Fig. 5 a) Calculated electronic band structure for a) SrPdAs and b) CaPdAs using the experimentally determined crystal structures.

The temperature-dependent electronic resistivities of annealed sintered pellets were measured to understand the influence of Sr/Ca alloying on the electronic properties, to identify any possible low-temperature phase transitions, and search for exotic electronic behavior (Fig. 6). The temperature dependent resistivities for all synthesized compounds increase with increasing temperature from 2-300K, indicative of metallic behaviour. This in agreement with our first principles calculations suggesting both CaPdAs and SrPdAs are metallic. The 2K resistivities ranged from 11 to 130 mΩ cm. The $Sr_{0.17}Ca_{0.83}PdAs$ was not included since it has the largest fraction of an unknown impurity phase. For all samples, there were no obvious discontinuities in the temperature dependent resistivities from 2-300K that would be expected from a hexagonal to orthorhombic distortion. Also, superconductivity was not observed in any sample down to 2K.

A second trend is apparent when comparing the resistivity values as a function of alloy concentration. SrPdAs and CaPdAs both have the lowest resistivities of 18 and 31 mΩ cm at room temperature, respectively. These resistivities are about one order of magnitude larger than the resistivity of SrPtAs.[21] As soon as either Ca or Sr are substituted into these phases, respectively, the resistivity values continuously increase, until it reaches a maximum at $Sr_{0.5}Ca_{0.5}PdAs$. This phase has about ~1 order of magnitude greater resistivity across all temperatures than SrPdAs and CaPdAs. $Sr_{0.5}Ca_{0.5}PdAs$ compound is the most Sr-rich phase which shows an orthorhombic distortion. It is well-established that alloy phases often have lower mobilities

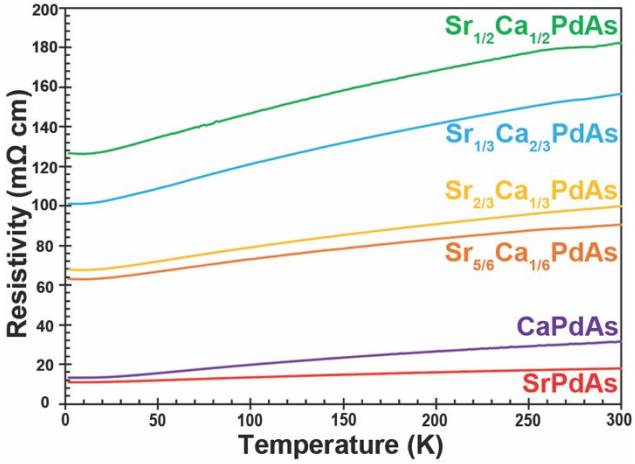

Fig. 6 The resistivity of $Sr_{1-x}Ca_xPdAs$ from $0 \le x \le 1$, but $Sr_{0.17}Ca_{0.83}PdAs$ was excluded due to the phase containing the largest unknown impurity. As concentrations of Sr and Ca are substituted into the phases the resistivities increase and $Sr_{0.5}Ca_{0.5}PdAs$ displays the largest resistivity.

compared to their end members, on account of the increased carrier scattering caused by the disruptions to the periodic atomic potential, a phenomenon known as the Nordheim rule.[36, 37] As a classic example, the mobilities of both p-doped and n-doped Si and Ge are much higher than $Si_{1-x}Ge_x$ alloys at the same doping levels.[38, 39]

4. Conclusions

Overall, we have elucidated in detail the changes in structure that occur in $Sr_{1-x}Ca_xPdAs$, as one varies, the alkaline earth content. We have detailed the structural changes across the alloy phases through the substitution of Sr and Ca in the unit cell, through the emergence of the orthorhombic distortion in the $Sr_{1/2}Ca_{1/2}PdAs$ phase. All phases display metallic resistivities from room temperature down to 2K, in close agreement with first principles calculations. The Sr/Ca alloy phases have higher resistivities than the SrPdAs and CaPdAs end members, which is in agreement with the Nordheim rule. Overall, this work establishes the correlation between the ionic radius of the alkaline earth element and the structural distortion in these layered honeycomb compounds, which is an essential goal for accessing the exotic phenomena in these compounds.

Conflicts of interest

There are no conflicts to declare.

Acknowledgements

This work was primarily supported by the Center for Emergent Materials, an NSF-funded MRSEC under award no. DMR-1420451. Partial support for transport measurements by M.R.S. was provided by AFOSR project no. FA9550-18-1-0335. J.E.G. acknowledges the Camille and Henry Dreyfus Foundation for partial support. D.W. gratefully acknowledges the financial support by the German Science Foundation DFG Research Fellowship (WE6 480/1). Y.W. and W.W. thank the Ohio Supercomputer Center for computer time under grant PAS0072.

References

1. M. G. Vergniory, L. Elcoro, C. Felser, N. Regnault, B. A. Bernevig and Z. Wang, A complete catalogue of high-quality topological materials, *Nature*, 2019, **566**, 480-485.
2. L. M. Schoop, F. Pielnhofer and B. V. Lotsch, Chemical Principles of Topological Semimetals, *Chem. Mater.*, 2018, **30**, 3155-3176.
3. M. Q. Arguilla, N. D. Cultrara, Z. J. Baum, S. Jiang, R. D. Ross and J. E. Goldberger, EuSn2As2: an exfoliatable magnetic layered Zintl-Klemm phase, *Inorg. Chem. Front.*, 2017, **4**, 378-386.
4. S. M. Young, S. Manni, J. Shao, P. C. Canfield and A. N. Kolmogorov, BaSn2: A wide-gap strong topological insulator, *Phys. Rev. B Condens. Matter*, 2017, **95**, 85116-85116.
5. S. Jiang, M. Q. Arguilla, N. D. Cultrara and J. E. Goldberger, Covalently-Controlled Properties by Design in Group IV Graphane Analogues, *Acc. Chem. Res.*, 2015, **48**, 144-151.
6. A. Molle, J. Goldberger, M. Houssa, Y. Xu, S.-C. Zhang and D. Akinwande, Buckled two-dimensional Xene sheets, *Nat. Mater.*, 2017, **16**, 163-169.
7. M. Q. Arguilla, J. Katoch, K. Krymowski, N. D. Cultrara, J. S. Xu, X. X. Xi, A. Hanks, S. Jiang, R. D. Ross, R. J. Koch, S. Ulstrup, A. Bostwick, C. Jozwiak, D. W. McComb, E. Rotenberg, J. Shan, W. Windl, R. K. Kawakami and J. E. Goldberger, NaSn2As2: An Exfoliatable Layered van der Waals Zintl Phase, *ACS Nano*, 2016, **10**, 9500-9508.
8. B. He, Y. X. Wang, M. Q. Arguilla, N. D. Cultrara, M. R. Scudder, J. E. Goldberger, W. Windl and J. P. Heremans, The Fermi surface geometrical origin of axis-dependent conduction polarity in layered materials, *Nat. Mater.*, 2019, **18**, 568-572.
9. Y. Wang, K. G. Koster, A. M. Ochs, M. R. Scudder, J. P. Heremans, W. Windl and J. E. Goldberger, The Chemical Design Principles for Axis-Dependent Conduction Polarity, *J. Am. Chem. Soc.*, 2020, **142**, 2812-2822.
10. I. Lee, F. G. Utermohlen, D. Weber, K. Hwang, C. Zhang, J. van Tol, J. E. Goldberger, N. Trivedi and P. C. Hammel, Fundamental Spin Interactions Underlying the Magnetic Anisotropy in the Kitaev Ferromagnet CrI3, *Phys. Rev. Lett.*, 2020, **124**, 17201.
11. B. Huang, G. Clark, E. Navarro-Moratalla, D. R. Klein, R. Cheng, K. L. Seyler, D. Zhong, E. Schmidgall, M. A. McGuire, D. H. Cobden, W. Yao, D. Xiao, P. Jarillo-Herrero and X. Xu, Layer-dependent ferromagnetism in a van der Waals crystal down to the monolayer limit, *Nature*, 2017, **546**, 270-273.
12. D. R. Klein, D. MacNeill, J. L. Lado, D. Soriano, E. Navarro-Moratalla, K. Watanabe, T. Taniguchi, S. Manni, P. Canfield, J. Fernández-Rossier and P. Jarillo-Herrero, Probing magnetism in 2D van der Waals crystalline insulators via electron tunneling, *Science*, 2018, **360**, 1218-1222.
13. T. Song, X. Cai, M. W.-Y. Tu, X. Zhang, B. Huang, N. P. Wilson, K. L. Seyler, L. Zhu, T. Taniguchi, K. Watanabe, M. A. McGuire, D. H. Cobden, D. Xiao, W. Yao and X. Xu, Giant tunneling magnetoresistance in spin-filter van der Waals heterostructures, *Science*, 2018, **360**, 1214-1218.
14. V. Carteaux, D. Brunet, G. Ouvrard and G. Andre, Crystallographic, magnetic and electronic structures of a new layered ferromagnetic compound Cr2Ge2Te6, *J. Phys.: Condens. Matter*, 1995, **7**, 69-87.
15. C. Gong, L. Li, Z. Li, H. Ji, A. Stern, Y. Xia, T. Cao, W. Bao, C. Wang, Y. Wang, Z. Q. Qiu, R. J. Cava, S. G. Louie, J. Xia and X. Zhang, Discovery of intrinsic ferromagnetism in two-dimensional van der Waals crystals, *Nature*, 2017, **546**, 265-269.
16. X. Li and J. Yang, CrXTe3 (X = Si, Ge) nanosheets: two dimensional intrinsic ferromagnetic semiconductors, *J. Mater. Chem. C*, 2014, **2**, 7071-7076.
17. K. L. Hodge and J. E. Goldberger, Transition Metal-Free Alkyne Hydrogenation Catalysis with BaGa2, a Hydrogen Absorbing Layered Zintl Phase, *J. Am. Chem. Soc.*, 2019, **141**, 19969-19972.
18. T.-N. Ye, Y. Lu, J. Li, T. Nakao, H. Yang, T. Tada, M. Kitano and H. Hosono, Copper-Based Intermetallic Electride Catalyst for Chemoselective Hydrogenation Reactions, *J. Am. Chem. Soc.*, 2017, **139**, 17089-17097.
19. J. Nagamatsu, N. Nakagawa, T. Muranaka, Y. Zenitani and J. Akimitsu, Superconductivity at 39 K in magnesium diboride, *Nature*, 2001, **410**, 63-64.
20. M. Imai, K. Nishida, T. Kimura and H. Abe, Superconductivity of Ca(Al0.5,Si0.5)2, a ternary silicide with the AlB2-type structure, *Appl. Phys. Lett.*, 2002, **80**, 1019-1021.
21. Y. Nishikubo, K. Kudo and M. Nohara, Superconductivity in the Honeycomb-Lattice Pnictide SrPtAs, *J. Phys. Soc. Jpn.*, 2011, **80**, 55002-55002.
22. M. D. Bojin and R. Hoffmann, The RE M E Phases, *Helv. Chim. Acta*, 2003, **86**, 1653-1682.
23. D. Johrendt and A. Mewis, Die elektronische Struktur ternärer Übergangsmetallpnictide. I. AlB2-Varianten, *Z. Naturforsch. B*, 1996, **51**, 655-664.
24. G. Michels, C. Huhnt, W. Scharbrodt, W. Schlabitz, E. Holland-Moritz, M. M. Abd-Elmeguid and A. Mewis, Temperature and pressure driven valence change in ternary Eu-pnictides, *Phys. B (Amsterdam, Neth.)*, 1995, **206-207**, 408-411.
25. D. Johrendt, R. Miericke and A. Mewis, Neue Pnictide mit modifizierten AIB2-Strukturen, *Z. Naturforsch. B*, 1996, **51**, 905.
26. G. Kresse, Ab initio molecular dynamics for liquid metals, *J. Non-Cryst. Solids*, 1995, **192-193**, 222-229.
27. G. Kresse and J. Hafner, Ab initio molecular-dynamics simulation of the liquid-metal--amorphous-semiconductor transition in germanium, *Phys. Rev. B Condens. Matter*, 1994, **49**, 14251-14269.
28. P. E. Blöchl, Projector augmented-wave method, *Phys. Rev. B Condens. Matter*, 1994, **50**, 17953-17979.
29. G. Kresse and D. Joubert, From ultrasoft pseudopotentials to the projector augmented-wave method, *Phys. Rev. B Condens. Matter*, 1999, **59**, 1758-1775.
30. S. L. Dudarev, G. A. Botton, S. Y. Savrasov, C. J. Humphreys and A. P. Sutton, Electron-energy-loss spectra and the structural stability of nickel oxide: An LSDA+U study, *Phys. Rev. B Condens. Matter*, 1998, **57**, 1505-1509.
31. H. Liu, B. Huang, J. Zhou, K. Wang, Y. Yu, W. Yang and S. Guo, Enhanced electron transfer and light absorption on imino polymer capped PdAg nanowire networks for efficient room-temperature dehydrogenation of formic acid, *J. Mater. Chem. A*, 2018, **6**, 1979-1984.

32. M. Van den Bossche, H. Grönbeck and B. Hammer, Tight-Binding Approximation-Enhanced Global Optimization, *J. Chem. Theory Comput.*, 2018, **14**, 2797-2807.
33. D. K. Wilson, B. Saparov and S. Bobev, Synthesis, Crystal Structures and Properties of the Zintl Phases Sr2ZnP2, Sr2ZnAs2, A2ZnSb2 and A2ZnBi2 (A = Sr and Eu), *Z. Anorg. Allg. Chem*, 2011, **637**, 2018-2025.
34. D. Johrendt and A. Mewis, Darstellung und kristallstrukturen der verbindungen SEPdAs (SE≡La-Lu), *J. Alloys Compd.*, 1992, **183**, 210-223.
35. A. Jain, S. P. Ong, G. Hautier, W. Chen, W. D. Richards, S. Dacek, S. Cholia, D. Gunter, D. Skinner, G. Ceder and K. a. Persson, The Materials Project: A materials genome approach to accelerating materials innovation, 2019).
36. G. L. Hall, Nordheim's Theory of the Resistivity of Alloys, *Phys. Rev.*, 1959, **116**, 604-605.
37. A. E. Asch and G. L. Hall, Quantum Theory of the Residual Electrical Resistivity of Disordered Alloys, *Phys. Rev.*, 1963, **132**, 1047-1057.
38. J. P. Dismukes, L. Ekstrom, E. F. Steigmeier, I. Kudman and D. S. Beers, Thermal and Electrical Properties of Heavily Doped Ge-Si Alloys up to 1300°K, *J. Appl. Phys.*, 1964, **35**, 2899-2907.
39. V. Oskar and G. Busch, Elektrische und magnetische Eigenschaften von Ge-Si Mischkristallen, *Helv. Phys. Acta*, 1960, **33**, 437-459.